

Molecular Physics



An International Journal at the Interface Between Chemistry and Physics

ISSN: (Print) (Online) Journal homepage: https://www.tandfonline.com/loi/tmph20

Hamiltonian based resonance-free approach for enabling very large time steps in multiple timescale molecular dynamics

Charlles R. A. Abreu & Mark E. Tuckerman

To cite this article: Charlles R. A. Abreu & Mark E. Tuckerman (2021) Hamiltonian based resonance-free approach for enabling very large time steps in multiple time-scale molecular dynamics, Molecular Physics, 119:19-20, e1923848, DOI: 10.1080/00268976.2021.1923848

To link to this article: https://doi.org/10.1080/00268976.2021.1923848

	Published online: 10 May 2021.
	Submit your article to this journal ぴ
ılıl	Article views: 286
Q ²	View related articles 🗹
CrossMark	View Crossmark data 🗗
4	Citing articles: 1 View citing articles 🗹



KLEIN SPECIAL ISSUE



Check for updates

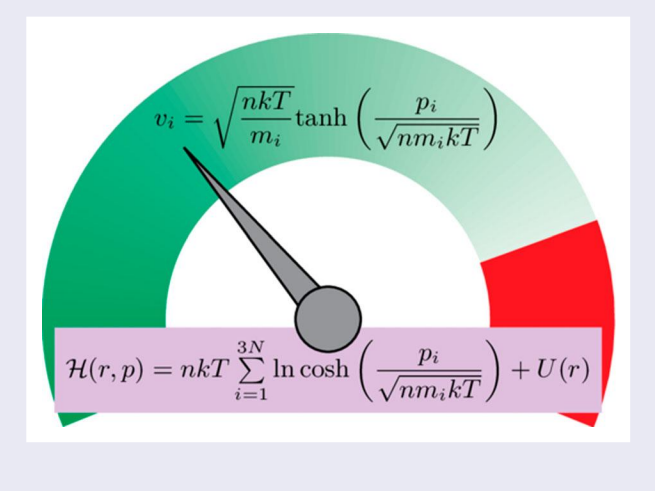
Hamiltonian based resonance-free approach for enabling very large time steps in multiple time-scale molecular dynamics

Charlles R. A. Abreu [©] and Mark E. Tuckerman [©] b,c,d

^aChemical Engineering Department, Escola de Química, Universidade Federal do Rio de Janeiro, Rio de Janeiro, RJ, Brazil; ^bDepartment of Chemistry, New York University, New York, NY, USA; Courant Institute of Mathematical Sciences, New York University, New York, NY, USA; ^dNYU-ECNU Center for Computational Chemistry at NYU Shanghai, Shanghai, People's Republic of China

ABSTRACT

Extended phase-space isokinetic methods in their deterministic [Minary et al., Phys. Rev. Lett. 93, 150201 (2004)] and stochastic forms [Leimkuhler et al., Mol. Phys. 111, 3579 (2013)] have proved tremendously successful in allowing multiple time-scale molecular dynamics simulations to be performed with very large time steps. These methods work by coupling the physical degrees of freedom to a set of Nosé-Hoover chain or Nosé-Hoover Langevin thermostats via an isokinetic constraint, which has the effect of avoiding resonance artifacts that plague multiple time-step algorithms. In this paper, we introduce a new resonance-free approach that achieves the same gains in time step but without the imposition of isokinetic constraints or the introduction of extended phase-space variables. Rather, we modify the physical Hamiltonian that effects the same regulation of resonances achieved by the isokinetic constraints. In so doing, we show that sampling errors can be controlled and performance improvements are possible within a simpler Hamiltonian framework. The method is demonstrated in simulations of the structure of liquid water and, in conjunction with enhanced sampling, in generation of the Ramachandran free-energy surface of the solvated alanine dipeptide.



ARTICLE HISTORY

Received 9 January 2021 Accepted 15 April 2021

KEYWORDS

Molecular dynamics; multiple time-stepping; resonance

1. Introduction

Multiple time-scale (MTS) integration [1–3] is an effective way of improving the efficiency of Molecular Dynamics (MD) simulations. In classical MD, MTS algorithms allow the most expensive computations, such as the evaluation of long-range van der Waals and electrostatic components of a force field, to be done less frequently than other components. This is possible because the

characteristic temporal fluctuations of such contributions are much smaller than those of both non-bonded interactions at short distances and bonded intramolecular forces. If the main goal of a simulation is to estimate freeenergy differences or other ensemble averages, then the maximum benefit one can obtain from MTS integration occurs when the largest step size and the correlation time of the system dynamics (i.e. the sampling period required

to obtain a series of uncorrelated configurations) have the same value. Although this is theoretically feasible in many situations, the full power of MTS integration has only recently been fully realised. The reason for this was the discovery of resonance artifacts [4-6], which limit the maximum attainable step size in a MTS run.

Various strategies to overcome the limitations of resonances have been proposed. One of the strategies, known as the mollified impulse method [7,8], relies on altering the slow part of the potential energy function. This is done by evaluating the corresponding forces at filtered positions, averaged along auxiliary trajectories which are, in turn, dictated by the fast part of the potential. A related method employs a generalised Langevin equation with a colored-noise kernel designed to mollify high-frequency components of the fast motion [9]. In another successful approach, the dynamics is altered via the introduction of a set of isokinetic constraints that couple the physical phase-space variables to a set of auxiliary variables in an extended-system approach [10-13]. The basic recipe consists in pairing the velocity of each physical degree of freedom in the system with a set of extended-space velocities, with a thermostat individually attached to each one of them. The combined kinetic energy of each physical and corresponding extra velocities is then constrained to be constant. In this way, the magnitude of any velocity can never exceed a certain value and, as a consequence, the likelihood of resonance and instability in the simulated dynamics decreases significantly. This procedure is not meant to reproduce the Maxwell-Boltzmann distribution of velocities of a canonical ensemble, however, it does generate the correct distribution of coordinates [10-13]. The method was originally formulated [10–12] with deterministic thermostats [14] and subsequently reformulated [13] with stochastic ones [15,16]. In the latter case, it is known as the SIN(R) method, standing for Stochastic Isokinetic Nosé-Hoover (RESPA) [13].

In the present paper, we introduce a new resonancefree approach that samples the same velocity distribution of the massive isokinetic framework without imposing constraints or introducing extended phase-space velocities apart from those used for standard thermostatting schemes such as Nosé-Hoover dynamics [17,18]. The method consists in replacing the kinetic energy term in the system Hamiltonian by a new momentum-dependent function whose main purpose is to restrict the velocities within a finite range, which we refer to here as regulation. The potential energy part of the Hamiltonian is kept unchanged. A consequence of the proposed regulation approach is that the velocity of an atom is no longer proportional to its momentum. We present two alternative thermostatting approaches, one based on the generalised equipartition theorem [19], which involves velocity-momentum products, and one based on a particular form entailing squared velocities [20]. The wellknown canonical equipartitioning is a limiting case in both approaches.

After the theoretical argument for the proposed framework is introduced, the remainder of the paper is structured as follows. A detailed phase-space analysis [21,22] is carried out in order to demonstrate that the Boltzmann-Gibbs distribution of coordinates is correctly sampled with massive Nosé-Hoover [17,18] thermostats as well as with their stochastic extensions known as Nosé-Hoover-Langevin (NHL) thermostats [15,16]. Following this analysis, we propose a middle-type integration scheme [23,24], in which the thermostat action takes place in the middle of the innermost loop, for multiple time-scale (MTS) integration of the regulated equations of motion. We then present a formulation of regulated dynamics for enhanced sampling and freeenergy landscape determination within the frameworks of Temperature-Accelerated MD [25]/ driven Adiabatic Free Energy Dynamics [26,27], and its metadynamicsbased extension known as Unified Free Energy Dynamics [28,29]. Finally, we carry out numerical calculations to verify the efficacy of regulation in avoiding resonance artifacts and its accuracy in the computation of configurational averages even when very large time steps are employed. For this demonstration, we simulate a fullyflexible water system with outer time steps $\Delta t \leq 90$ fs and obtain free energy surfaces for dihedral angles of alanine dipeptide in aqueous solution with $\Delta t \leq 120$ fs using the enhanced sampling-based formulation.

In the appendix, we determine the probability densities and corresponding moments involved in the regulated ensemble and demonstrate that the regulated version of the massive NHL method not only reproduces the isokinetic ensemble but is also closely related to the SIN(R) method [13] in terms of dynamics.

2. Theory

2.1. Molecular dynamics in the canonical ensemble

For a classical system with coordinates $r \in \mathbb{R}^{N_f}$, where N_f is the number of degrees of freedom, we are often interested in computing canonical-ensemble averages of a purely configurational property, $A(\mathbf{r})$, as

$$\langle A \rangle = \frac{1}{Z} \int A(r) e^{-U(r)/kT} dr,$$
 (1)

where T is the temperature, k is the Boltzmann constant, U(r) is a potential energy function, and Z is the configurational partition function. This is usually accomplished

$$\mathcal{H}(r,p) = U(r) + \sum_{i=1}^{N_f} \frac{p_i^2}{2m_i}$$
 (2)

and exploring the phase space by means of some canonical (constant NVT) dynamics method. In this expression, p_i is a momentum conjugate to r_i , and m_i is the mass associated with a degree of freedom i. This procedure samples the canonical probability density $\rho(r, p) \propto$ $e^{-\mathcal{H}(r,p)/kT}$ up to small systematic deviations introduced by the numerical temporal discretisation [30-33]. As a result, coordinates are sampled with the desired probabilities and, at the same time, each momentum p_i fluctuates according to a normal distribution whose mean is zero and standard deviation is $\sqrt{m_i kT}$.

In Hamiltonian dynamics, as well as in most non-Hamiltonian methods devised to sample the canonical ensemble, the velocity of a particle is the derivative of \mathcal{H} with respect to its momentum, that is, since $\dot{r}_i = \partial \mathcal{H}/\partial p_i$, and $v_i = \dot{r}_i$, it follows that

$$v_i = \frac{\partial \mathcal{H}}{\partial p_i}. (3)$$

Therefore, in a simulation with a standard Hamiltonian of the form given in Equation (2), in which $v_i = \frac{p_i}{m_i}$, a large displacement will take place whenever the absolute value of some momentum increases excessively due to the action of a large force. Time discretisation can cause such forces to emerge due to, for instance, spurious atomic overlaps, thus causing numerical instability. Massive isokinetic methods [10–13] manage to avoid this problem by setting an upper bound to the kinetic energy of every degree of freedom. Therefore, the largest singlestep displacement that a coordinate r_i can undergo during a massive isokinetic simulation is $c_i \delta t$, where δt is the size of each time step – or each inner time step, in the case of a MTS simulation – and c_i is the speed limit imposed on such a degree of freedom (analogous to the role played by the speed of light in Special Relativity). A side-effect of this strategy is that the probability distribution of velocities is no longer Gaussian but has a particular form that depends on the number of thermostats attached to each degree of freedom [20]. On the one hand, the details of the velocity and momentum distributions are not particularly relevant if one is only interested in configurational averages. On the other hand, mixing times can actually be affected, thus altering the efficiency with which the coordinate space is sampled. We have shown [20] that, on average, each atom is slower within isokinetic dynamics than it would be in standard canonical/thermostatted molecular dynamics at the same temperature.

2.2. New Hamiltonian for regulated isothermal dynamics

Inspired by the massive isokinetic methods [10–13,34], we propose a new approach to impose a speed limit c_i on each degree of freedom in a dynamical system. This approach, which we will refer to as regulated dynamics, consists in using the following modified Hamiltonian:

$$\mathcal{H}_n(r,p) = U(r) + nkT \sum_{i=1}^{N_f} \ln \cosh \left(\frac{p_i}{\sqrt{nm_i kT}} \right), \quad (4)$$

where n > 0 is an arbitrary parameter.

The new Hamiltonian shares important properties with that of Equation (2). For instance, \mathcal{H}_n is an even function of every p_i and is, therefore, invariant to changes in sign of p_i , i.e. $p_i \rightarrow -p_i$. It is also separable in coordinates and momenta, which makes the marginal equilibrium distributions of *r* and *p* independent of each other. Finally, the marginal distribution of each component p_i of p is independent of that of p_i for $i \neq j$. Together with the condition that $e^{-\mathcal{H}_n(r,p)/kT} \to 0$ when any $|p_i| \to$ ∞ , such separability renders valid [35] the generalised equipartition theorem [19], which states that

$$\left\langle p_i \frac{\partial \mathcal{H}_n}{\partial p_i} \right\rangle = kT. \tag{5}$$

Another desirable feature of \mathcal{H}_n is that it approaches the standard Hamiltonian when n increases. This becomes clear by observing the series expansion

$$n \ln \cosh\left(\frac{x}{\sqrt{n}}\right) = \frac{x^2}{2} - \frac{x^4}{12n} + \frac{x^6}{45n^2} + \mathcal{O}(x^8). \quad (6)$$

If a constant-NVT simulation is set up with the new Hamiltonian, the coordinate distribution that will be sampled is proportional to $e^{-U(r)/kT}$, as it was designed to do, while each momentum p_i will be sampled according to a probability density given by

$$\rho_n(p_i) = \frac{\Gamma\left(\frac{n+1}{2}\right)}{\Gamma\left(\frac{n}{2}\right)\sqrt{\pi n m_i k T}} \operatorname{sech}^n\left(\frac{p_i}{\sqrt{n m_i k T}}\right), \quad (7)$$

where $\Gamma(\cdot)$ is the complete gamma function. This probability density, whose normalisation constant is obtained in Appendix 1, is depicted in the top row of Figure 1 for various integer values of *n*. The tendency toward a normal distribution with increasing n is evident. The figure also depicts, in the middle row, the relation between velocity and momentum for the same values of *n*. Such a relation, obtained from Equations (3) and (4), is

$$v_i = c_i \tanh\left(\frac{p_i}{m_i c_i}\right),\tag{8}$$

where the limiting speed c_i is given by

$$c_i = \sqrt{\frac{nkT}{m_i}}. (9)$$

It is interesting to observe the distribution of velocities, whose form is derived in Appendix 1 and is given by

$$\varrho_{n}(v_{i}) = \begin{cases} \frac{1}{c_{i}} \frac{\Gamma\left(\frac{n+1}{2}\right)}{\Gamma\left(\frac{n}{2}\right)\sqrt{\pi}} \left(1 - \frac{v_{i}^{2}}{c_{i}^{2}}\right)^{\frac{n}{2} - 1} & \text{if } v_{i}^{2} \leq c_{i}^{2} \\ 0 & \text{otherwise} \end{cases}$$

$$(10)$$

This distribution is depicted in the bottom row of Figure 1 for the same values of n as shown previously. With $n \in \mathbb{N}$, such a distribution becomes identical to that corresponding to massive isokinetic dynamics [20], with parameter n substituting for the number of thermostats attached to each degree of freedom. One important aspect of this distribution, which will be essential in the forthcoming discussion about thermostat algorithms, is the special form of the kinetic energy equipartition it implies (see Appendix 1), which is, specifically,

$$\langle m_i v_i^2 \rangle = \frac{n}{n+1} kT. \tag{11}$$

The standard canonical-ensemble equipartitioning is approached only as $n \to \infty$, and the result is approached from below, meaning that particles are slower, on average, than their counterparts in a canonical ensemble at the same temperature. We have already observed this fact in the case of massive isokinetic dynamics methods [20], with implications in their capability of producing uncorrelated samples for configurational property determination. With a single thermostat per degree of freedom, for instance, the mean kinetic energy of the system is only half the value corresponding to a standard canonical ensemble. Following the same principle, it is straightforward to devise a Hamiltonian that would lead to the standard equipartition equation regardless of the value of n. It is

$$\mathcal{H}_{n}^{\text{eqp}}(r,p) = U(r) + nkT \sum_{i=1}^{N_f} \ln \cosh \left(\sqrt{\frac{n+1}{n^2 m_i k T}} p_i \right).$$
(12)

However, as we will show in this article through numerical tests (see Section 4.1), such an alternative Hamiltonian introduces new artifacts that compromise

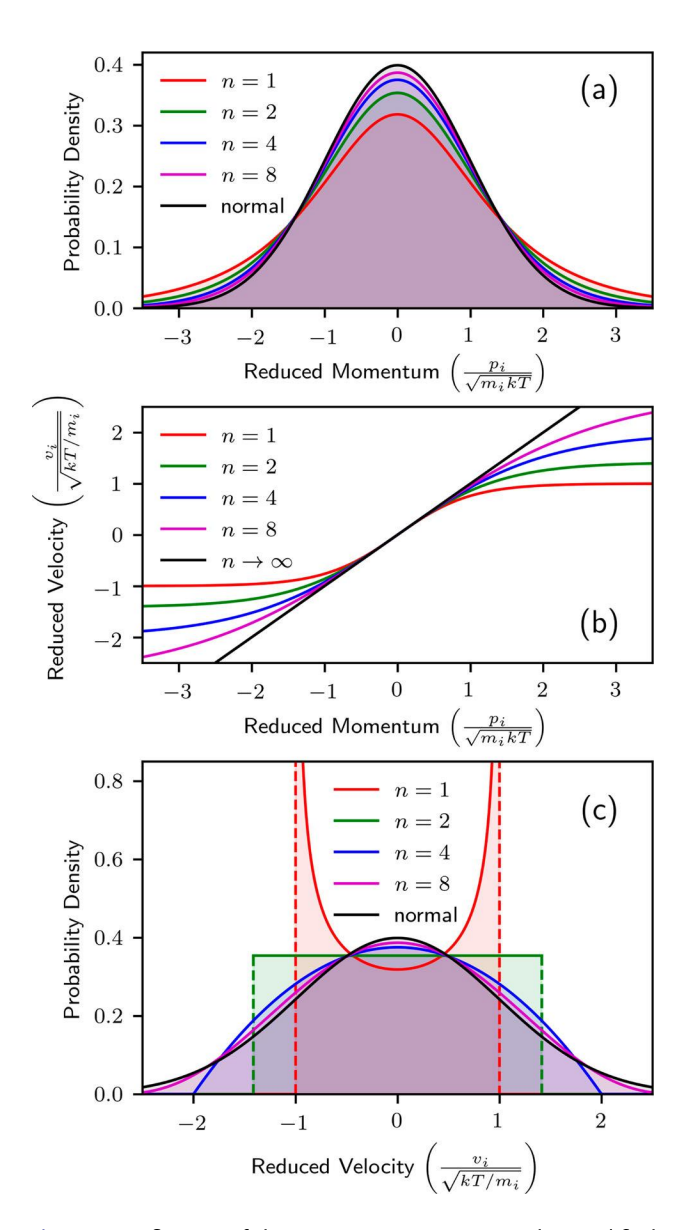


Figure 1. Influence of the parameter n present in the modified Hamiltonian \mathcal{H}_n as defined in Equation (4) on the probability distributions and velocity-momentum relation involved in the regulated dynamics ensemble. (a) The momentum probability density, Equation (7). (b) The velocity of a degree of freedom as a function of its momentum, Equation (8). (c) The velocity probability density, Equation (10).

its performance in multiple time-scale simulations as compared to the performance of Equation (4). In an attempt to understand why this is the case, we can compare Figures 1(b) and 2, which shows the velocity-momentum relationship that results from $\mathcal{H}_n^{\text{eqp}}$ via $\dot{r}_i = \partial \mathcal{H}^{\text{eqp}}/\partial p_i$. The straight line that appears in both figures represents the conventional relation $v_i = p_i/m_i$. Note that all curves in Figure 1(b) collapse onto this straight line in the region around $p_i = 0$, where the peak of the momentum distribution lies. In contrast, as Figure 2 shows, requiring that $\langle m_i v_i^2 \rangle = kT$ regardless of the n

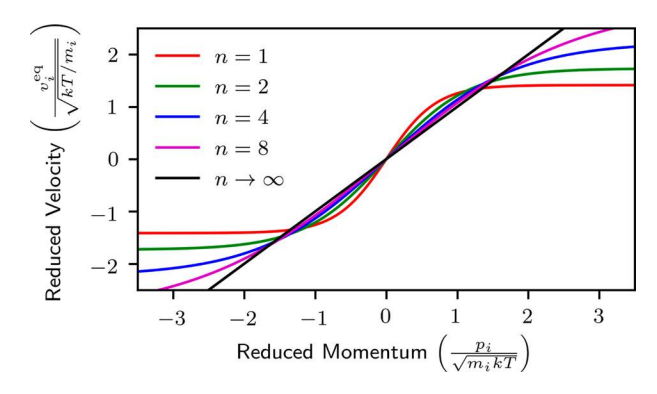


Figure 2. The velocity-momentum relation corresponding to the alternative Hamiltonian $\mathcal{H}_n^{\text{eqp}}$ defined in Equation (12), which yields standard energy equipartition regardless of the value of parameter n.

parameter value implies that v_i will always deviate from p_i/m_i when n is small (see, e.g. the curve for n=1). For these reasons, requiring that the standard kinetic energy equipartitioning be satisfied is not pursued further in our proposed methods.

In the proceeding sections, we will describe simulation methods that aim to reproduce a canonical distribution of the new Hamiltonian. First, we employ a massive version of an existing thermostat algorithm and show that it simply relies on the validity of the generalised equipartition theorem, Equation (5), as the basis for proper thermostatting. Next, we devise a new algorithm that relies on the particular equipartitioning in Equation (11) instead. A marked difference between these two principles is that the quantity subject to equipartitioning in Equation (5) is unbounded due to the presence of p_i , whereas its counterpart in Equation (11) has $m_i c_i^2$ as an upper bound. For this reason, we will classify methods based on Equation (5) as semi-regulated, as a way of distinguishing them from those based on Equation (11). Finally, although it is beyond the scope of this article, it is worth mentioning that higher-order central moments (see Appendix 1) can also be used for implementing thermostatting schemes, as in, for example, the Generalised Gaussian Moment method [36].

3. Methods

3.1. Semi-regulated Nosé-Hoover-Langevin dynamics

In order to derive equations of motion for a regulated NVT dynamics in the physical phase space (r,p), we employ a massive version of the Nosé-Hoover-Langevin (NHL) method [15,16]. This begins by extending the phase space with N_f extra pairs of coordinates $\eta \in \mathbb{R}^{N_f}$ and conjugate momenta $p_{\eta} \in \mathbb{R}^{N_f}$. An inertial parameter Q_{η_i} is associated with each degree of freedom. The

dynamics of the NHL method is described by a system of stochastic differential equations (SDEs)

$$dr_i = v_i dt = c_i \tanh\left(\frac{p_i}{m_i c_i}\right) dt,$$
 (13a)

$$dp_i = \left(F_i - \frac{p_{\eta_i}}{Q_{n_i}} p_i\right) dt, \quad \text{and}$$
 (13b)

$$dp_{\eta_i} = (p_i \nu_i - kT) dt - \gamma p_{\eta_i} dt + \sqrt{2\gamma Q_{\eta_i} kT} dW_{\eta_i},$$
(13c)

where $F_i = -\partial U/\partial r_i$ is the force exerted on i, γ is a friction constant, and dW_{η_i} denotes an infinitesimal increment of a Wiener process. Note that the velocity v_i is computed via Equation (8), which is the single difference between the regulated and standard versions of the massive NHL method. An equation $d\eta_i = (p_{\eta_i}/Q_{\eta_i})dt$ for each i could have been included as well, but it can be ignored in practice, as it has no influence on the dynamics in the physical phase space. Nevertheless, such an equation is important from a theoretical standpoint when it comes to demonstrating that the physical phase space is correctly sampled in accordance with $e^{-\mathcal{H}_n(r,p)/kT}$.

The main advantage of the proposed method becomes clear in the context of multiple time-scale (MTS) integration algorithms. We begin, however, by presenting a single time-scale integration scheme, which can be easily extended to MTS methods. As has been demonstrated in recent years [23,24,37–39], middle-type integration schemes are very accurate at reproducing the distribution of coordinates at the expense of the accuracy in the velocity distribution. This is particularly appealing in the present context. Leimkuhler and Matthews [40] presented a middle-type integrator for the NHL method, which we adapt here for a massive thermostatting approach based on the modified Hamiltonians described previously.

By writing the equations of motion as $\dot{\mathbf{x}} = \mathcal{L}_{\mathbf{x}}\mathbf{x}$, where \mathbf{x} is the vector of all extended phase-space variables and $\mathcal{L}_{\mathbf{x}}$ represents a Lie derivative (i.e. a non-Hamiltonian extension of the Liouville operator), we can partition $\mathcal{L}_{\mathbf{x}} = \mathcal{L}_r^{\mathrm{tr}} + \mathcal{L}_p^{\mathrm{tr}} + \mathcal{L}_p^{\mathrm{sc}} + \mathcal{L}_{p_{\eta}}^{\mathrm{tr}} + \mathcal{L}_{p_{\eta}}^{\mathrm{ou}}$, where $\mathcal{L}_r^{\mathrm{tr}} = \sum_{i=1}^{N_f} v_i \frac{\partial}{\partial r_i}$, $\mathcal{L}_p^{\mathrm{tr}} = \sum_{i=1}^{N_f} F_i \frac{\partial}{\partial p_i}$, $\mathcal{L}_p^{\mathrm{sc}} = -\sum_{i=1}^{N_f} \frac{p_{\eta_i}}{Q_{\eta_i}} p_i \frac{\partial}{\partial p_i}$, $\mathcal{L}_p^{\mathrm{tr}} = \sum_{i=1}^{N_f} (p_i v_i - kT) \frac{\partial}{\partial p_{\eta_i}}$, and $\mathcal{L}_{p_{\eta}}^{\mathrm{ou}}$ corresponds to an Ornstein-Uhlenbeck stochastic process applied to p_{η} . Superscripts 'tr' and 'sc' stand for translation and scaling, respectively. The integration step of the middle-type [23] method presented here, which derives from the usual Trotter-Suzuki [41,42] or Strang [43] splitting solution, is expressed as a classical propagator [44] given by

$$e^{\Delta t \mathcal{L}_{\mathbf{x}}} \approx e^{\frac{\Delta t}{2} \mathcal{L}_{p}^{\text{tr}}} e^{\frac{\Delta t}{2} \mathcal{L}_{r}^{\text{tr}}} e^{\Delta t \mathcal{L}_{\text{bath}}} e^{\frac{\Delta t}{2} \mathcal{L}_{r}^{\text{tr}}} e^{\frac{\Delta t}{2} \mathcal{L}_{p}^{\text{tr}}},$$
 (14)

where $e^{\Delta t \mathcal{L}_{bath}} = e^{\frac{\Delta t}{2} \mathcal{L}_{p\eta}^{tr}} e^{\frac{\Delta t}{2} \mathcal{L}_{p}^{sc}} e^{\Delta t \mathcal{L}_{p\eta}^{ou}} e^{\frac{\Delta t}{2} \mathcal{L}_{p}^{sc}} e^{\frac{\Delta t}{2} \mathcal{L}_{p\eta}^{tr}}$. The effects of all these propagators on each degree of freedom i can be expressed as

$$e^{t\mathcal{L}_r^{tr}}: r_i = r_i^0 + v_i^0 t, \tag{15}$$

$$e^{t\mathcal{L}_p^{tr}}: p_i = p_i^0 + F_i^0 t,$$
 (16)

$$e^{t\mathcal{L}_{p_{\eta}}^{tr}}: p_{\eta_{i}} = p_{\eta_{i}}^{0} + (p_{i}^{0}v_{i}^{0} - kT)t,$$
 (17)

$$e^{t\mathcal{L}_p^{sc}}: p_i = p_i^0 e^{-\frac{p_{\eta_i}^0}{Q_{\eta_i}}t}, \quad \text{and}$$
 (18)

$$e^{t\mathcal{L}_{p\eta}^{\text{ou}}}: p_{\eta_i} = p_{\eta_i}^0 e^{-\gamma t} + \sqrt{Q_{\eta_i} kT(1 - e^{-2\gamma t})} R_{\eta_i},$$
 (19)

where $v_i^0 = c_i \tanh(\frac{p_i^0}{m_i c_i})$, R_{η_i} is an independent random variate following the standard normal probability distribution, a 0 superscript denotes the initial condition encountered by a propagator, and t corresponds to the time span of its action. Implementing these solutions is straightforward and follows the 'direct translation' technique of Ref. [3], once a computer code is available for evaluating the forces at every time step.

As done in Ref. [13], we show that the Boltzmann-Gibbs distribution of coordinates is correctly obtained. For this purpose, we derive the equilibrium distribution of the method in its deterministic limit, with $\gamma=0$. We then show that the stochastic contribution maintains the distribution. The deterministic version of Equations (13) is a massive Nosé-Hoover [17,18] thermostat applied to \mathcal{H}_n as expressed in Equation (4). The system is a non-Hamiltonian one that conserves an energy function defined as

$$H_n(r, p, \eta, p_{\eta}) = \mathcal{H}_n(r, p) + \sum_{i=1}^{N_f} \left(kT\eta_i + \frac{p_{\eta_i}^2}{2Q_{\eta_i}} \right).$$
 (20)

A family of equations of motion devised to preserve H_n can be written in the general form [45]

$$\dot{\mathbf{x}} = \mathbf{B} \frac{\partial H_n}{\partial \mathbf{x}},\tag{21}$$

where \mathbf{x} is the vector of all extended phase-space variables, \mathbf{B} is a skew-symmetric, matrix-valued function of \mathbf{x} , and $\frac{\partial}{\partial \mathbf{x}}$ is the gradient operator. By virtue of the chain rule, the time derivative of any scalar function $f(\mathbf{x})$ is given by $\dot{f} = \dot{\mathbf{x}}^t \frac{\partial f}{\partial \mathbf{x}} = (\frac{\partial H_n}{\partial \mathbf{x}})^t \mathbf{B}^t (\frac{\partial f}{\partial \mathbf{x}})$. When $f = H_n$, this expression is a quadratic form that becomes identically null whenever its defining matrix is skew-symmetric. Hence, $\dot{H}_n = 0$. For a massive thermostatting approach, both \mathbf{B} and $\frac{\partial H_n}{\partial \mathbf{x}}$ can be cast in block form, with \mathbf{B} having a block-diagonal structure. In the case of a Nosé-Hoover dynamics, the main-diagonal blocks defined for

each degree of freedom i are

$$\mathbf{B}_{i,i} = \begin{bmatrix} 0 & 1 & 0 & 0 \\ -1 & 0 & 0 & -p_i \\ 0 & 0 & 0 & 1 \\ 0 & p_i & -1 & 0 \end{bmatrix} \quad \text{and}$$

$$\frac{\partial H_n}{\partial \mathbf{x}_i} = \begin{bmatrix} -F_i \\ v_i \\ kT \\ \underline{p}_{\eta,i} \end{bmatrix}. \tag{22}$$

Note that the entries of $\frac{\partial H_n}{\partial \mathbf{x}_i}$ are the derivatives of H_n with respect to r_i , p_i , η_i , and p_{η_i} , respectively. The present development will prove useful again in Section 3.2, where we derive a different method that also preserves H_n . It follows from Equations (21) and (22) that

$$\dot{r}_i = v_i, \tag{23a}$$

$$\dot{p}_i = F_i - \frac{p_{\eta_i}}{Q_{n_i}} p_i, \tag{23b}$$

$$\dot{\eta}_i = \frac{p_{\eta_i}}{Q_{\eta_i}}, \quad \text{and}$$
(23c)

$$\dot{p}_{n_i} = v_i p_i - kT, \tag{23d}$$

which is an ODE system that matches Equations (13) in the deterministic limit. By contrasting Equation (23d) with Equation (5), we realise that the method described above is founded on the generalised equipartition theorem.

In order to apply the phase-space analysis method developed in Refs. [21,22], we need to determine the phase space compressibility, which is defined as $\kappa = \nabla_{\mathbf{x}} \cdot \dot{\mathbf{x}}$. In the case of Equation (23),

$$\kappa = -\sum_{i=1}^{N_f} \frac{p_{\eta_i}}{Q_{\eta_i}} = -\sum_{i=1}^{N_f} \dot{\eta}_i.$$
 (24)

A phase-space flow like Equation (21) takes place in a manifold $H_n(\mathbf{x}) = H_n^0$, where the constant H_n^0 depends on the initial condition. If this dynamics is ergodic and H_n is the only conserved quantity, then the partition function of the resulting ensemble can be expressed as [21,22]

$$\Omega = C \int \delta \left(H_n(\mathbf{x}) - H_n^0 \right) \sqrt{g} \, d\mathbf{x}, \tag{25}$$

where $\delta(\cdot)$ is the Dirac delta function, \sqrt{g} is a metric determinant, and C is the proper statistical-mechanical prefactor, whose form is irrelevant for the present analysis. For a system with a global thermostat and no external forces, quantities related to the sum of all momenta for

each spatial dimension would be preserved. However, this conservation law is no longer present when massive and/or stochastic thermostats are employed. Thus, according to Refs. [21,22], we must simply substitute e^{-w} for \sqrt{g} in Equation (25), where w is defined such that $\dot{w} = \kappa$ [21,22]. Therefore, it follows from Equation (24) that

$$\Omega = C \int \delta \left(H_n(\mathbf{x}) - H_n^0 \right) e^{\sum_{i=1}^{N_f} \eta_i} d\mathbf{x}$$

$$= C^* \int e^{-\mathcal{H}_n(r,p)/kT} e^{-\|p_\eta\|^2/(2Q_{\eta_i}kT)} dr dp dp_\eta, \quad (26)$$

where integration over all η_i has been carried out after replacing $H_n(\mathbf{x})$ using Equation (20). This result shows that the marginal distribution in the physical phase space is proportional to $e^{-\mathcal{H}_n(r,p)/kT}$. In addition, each extended-space momentum p_{η_i} follows a normal distribution whose variance is $Q_{\eta_i}kT$. As shown in Ref. [13] by means of the Fokker-Planck equation, the latter condition is sufficient for the complete set of stochastic equations of motion to maintain the limiting distribution implied by the partition function above.

3.2. Regulated Nosé-Hoover-Langevin dynamics

We now propose a different version of the massive NHL algorithm whose thermostatting capability relies on the special form of the kinetic energy equipartitioning expressed in Equation (11). Based on the developments of Section 3.1, we begin by describing the deterministic version of the method before including a Langevintype thermostat. The new equations of motion can be obtained simply by modifying some entries of the matrix **B** presented in Equations (21) and (22) while maintaining its skew-symmetric and block-diagonal structures. Each block in the main diagonal of the modified matrix is

$$\mathbf{B}_{i,i} = \begin{bmatrix} 0 & 1 & 0 & 0 \\ -1 & 0 & 0 & -m_i v_i \\ 0 & 0 & 0 & 1 - \frac{v_i^2}{c_i^2} \\ 0 & m_i v_i & -1 + \frac{v_i^2}{c_i^2} & 0 \end{bmatrix}. \quad (27)$$

As a result, given that $c_i^2 = nkT/m_i$, Equation (21) becomes

$$\dot{r}_i = v_i, \tag{28a}$$

$$\dot{p}_i = F_i - \frac{p_{\eta_i}}{Q_{\eta_i}} m_i \nu_i, \tag{28b}$$

$$\dot{\eta}_i = \left(1 - \frac{v_i^2}{c_i^2}\right) \frac{p_{\eta_i}}{Q_{\eta_i}}, \quad \text{and}$$
 (28c)

$$\dot{p}_{\eta_i} = \frac{n+1}{n} m_i v_i^2 - kT.$$
 (28d)

Due to the skew symmetry of **B**, it is straightforward to conclude that the equations above preserve the extended energy defined in Equation (20). The phase-space compressibility they imply is $\kappa = -\sum_{i=1}^{N_f} \frac{p_{\eta_i}}{Q_{\eta_i}} m_i \frac{\partial v_i}{\partial p_i}$. From Equation (8), it follows that

$$\frac{\partial v_i}{\partial p_i} = \frac{1}{m_i} \left[1 - \tanh^2 \left(\frac{p_i}{m_i c_i} \right) \right] = \frac{1}{m_i} \left(1 - \frac{v_i^2}{c_i^2} \right). \tag{29}$$

Therefore,

$$\kappa = -\sum_{i=1}^{N_f} \frac{p_{\eta_i}}{Q_{\eta_i}} \left(1 - \frac{v_i^2}{c_i^2} \right) = -\sum_{i=1}^{N_f} \dot{\eta}_i.$$
 (30)

Remarkably, this result guarantees that the modified method will produce the same partition function given in Equation (26) and, therefore, the same limiting distribution in the physical phase space. We are now ready to include the stochastic contributions to the equations of motion, which then become

$$dr_i = v_i dt = c_i \tanh\left(\frac{p_i}{m_i c_i}\right) dt,$$
 (31a)

$$dp_i = \left(F_i - \frac{p_{\eta_i}}{Q_{n_i}} m_i v_i\right) dt, \quad \text{and}$$
 (31b)

$$dp_{\eta_i} = \left(\frac{n+1}{n} m_i v_i^2 - kT\right) dt$$
$$- \gamma p_{\eta_i} dt + \sqrt{2\gamma Q_{\eta_i} kT} dW_{\eta_i}.$$
(31c)

Here we have, once again, omitted the decoupled equation of motion of each variable η_i . Numerical integration of this new system of equations can be done in a manner similar to that of Equations (13), with only two differences. The first lies in the action of the p_n translation propagator, which is now expressed as

$$e^{t\mathcal{L}_{p_{\eta}}^{tr}}: p_{\eta_{i}} = p_{\eta_{i}}^{0} + \left[\frac{n+1}{n}m_{i}(\nu_{i}^{0})^{2} - kT\right]t.$$
 (32)

The second difference lies in the evaluation of the *p* scaling propagator, whose action is determined from the analytical solution of the differential equation

$$\dot{p}_i = -\frac{p_{\eta_i}}{Q_{\eta_i}} m_i v_i = -\frac{p_{\eta_i}}{Q_{\eta_i}} m_i c_i \tanh\left(\frac{p_i}{m_i c_i}\right). \tag{33}$$

By changing variables from p_i to $y_i = \sinh(\frac{p_i}{m_i c_i})$, the differential equation above becomes $\dot{y}_i = -\frac{p_{\eta_i}}{Q_{n_i}} y_i$, whose solution is a simple scaling of y_i . Therefore, by changing back from y_i to p_i , the action of $e^{t\mathcal{L}_p^{sc}}$ becomes

$$e^{t\mathcal{L}_p^{sc}}: p_i = m_i c_i \operatorname{arcsinh} \left[\sinh \left(\frac{p_i^0}{m_i c_i} \right) e^{-\frac{p_{\eta_i}^0}{Q_{\eta_i}} t} \right].$$
 (34)

With these two propagators replacing their counterparts, a single time-scale integration step can again be designed exactly as in Equation (14).

3.3. Multiple time-scale numerical integration

To come up with numerical integrators based on the reference system propagator algorithm (RESPA) [2], we can split the force on each degree of freedom *i* into a sum of M terms as $F_i = \sum_{k=1}^{M} F_i^{[k]}$. By convention, the characteristic time scale of each term increases with index k, meaning that $F_i^{[1]}$ and $F_i^{[M]}$ are the fastest and the slowest force components, respectively. Traditionally, equations of motion for constant-NVT dynamics with this type of force splitting are integrated by using one of the extended-dynamics schemes developed in Ref. [3]. For instance, in the XO-RESPA (eXtended-Outer-RESPA) scheme, thermostat-related propagators such as $e^{\Delta t \mathcal{L}_{bath}}$ in Equation (14), are evaluated first and last using the largest time step. More recently, middle-type integration [23] has also been used successfully in the context of resonance-free, multiple time-scale methods [20,24]. In a recursive fashion, a full time step of our middle-RESPA integration scheme can be written as

$$e^{\Delta t \mathcal{L}_{\mathbf{x}}} \approx \mathcal{G}_{M}(\Delta t),$$
 (35)

where \mathcal{G}_M belongs to a family of nested operators

$$\mathcal{G}_{k}(\delta t) = \begin{cases} e^{\frac{\delta t}{2} \mathcal{L}_{p}^{[k]}} \left[\mathcal{G}_{k-1} \left(\frac{\delta t}{n_{k}} \right) \right]^{n_{k}} e^{\frac{\delta t}{2} \mathcal{L}_{p}^{[k]}} & \text{if } k > 1, \\ e^{\frac{\delta t}{2} \mathcal{L}_{p}^{[1]}} e^{\frac{\delta t}{2} \mathcal{L}_{r}^{\text{tr}}} e^{\delta t \mathcal{L}_{\text{bath}}} e^{\frac{\delta t}{2} \mathcal{L}_{r}^{\text{tr}}} e^{\frac{\delta t}{2} \mathcal{L}_{p}^{\text{tr}}} & \text{if } k = 1. \end{cases}$$

$$(36)$$

Therefore, every step of size δt taken at a time scale kentails n_k substeps of size $\delta t/n_k$ taken, in turn, at the k-1 scale. This recursion comes to an end at the fastest time scale, k = 1, in which the coordinate moves and the thermostatting take place. The Lie derivative $\mathcal{L}_p^{[k]}$ is equal to $\sum_{i=1}^{N_f} F_i^{[k]} \frac{\partial}{\partial p_i}$, so that its corresponding exponential propagator acts on each degree of freedom i as a momentum translation akin to that in Equation (16) but involving the component $F_i^{[k]}$ only. In Ref. [24], the integrator above was applied to the SIN(R) method and named as 'VV-Middle-SIN(R)'.

3.4. Unified free energy dynamics

A challenge often faced in computational chemistry is the calculation of a free energy or potential of mean force (PMF) surface via $\phi(s) = -kT \ln \rho(s)$, where $\rho(s)$ is the marginal probability density for the observation of any configuration r for which q(r) = s, with $q: \mathbb{R}^{N_f} \mapsto$ $\mathbb{R}^{N_{\nu}}$ representing a set of N_{ν} collective variables capable of distinguishing important free-energy basins and saddle-point regions. Here, $s \in \mathbb{R}^{N_v}$ denotes a set of coarse-grained variables that parameterise the marginal probability distribution. With no loss of generality, these variables will be considered here as dimensionless and equally ranged. For a separable Hamiltonian and a canonical ensemble, the probability density in question is given by

$$\rho(s) = \frac{1}{\Xi} \int e^{-U(r)/kT} \prod_{\alpha=1}^{N_{\nu}} \delta(q_{\alpha}(r) - s_{\alpha}) dr, \quad (37)$$

where $\Xi = \int e^{-U(r)/kT} dr$ is the configurational partition function, and $\delta(\cdot)$ is the Dirac delta function, which is the zero-variance limit of the Gaussian probability density. Therefore,

$$\delta\left(q_{\alpha}(r) - s_{\alpha}\right) = \lim_{\kappa_{\alpha} \to \infty} \sqrt{\frac{\kappa_{\alpha}}{2\pi k T}} e^{-\frac{\kappa_{\alpha}}{2kT} \left[q_{\alpha}(r) - s_{\alpha}\right]^{2}}. (38)$$

A suitable approximation to the δ -function is obtained by assigning a large but finite value to every parameter κ_{α} , so that the problem can be restated as the determination of a function $\phi_{\kappa}(s) = -kT \ln \rho_{\kappa}(s)$, where $\kappa \in \mathbb{R}^{N_{\nu}}$ and $\rho_{\kappa}(s)$ is the marginal probability density of s, obtained by integrating over r the joint probability density $\rho_{\kappa}(r,s) =$ $(1/\Xi_{\kappa}) e^{-U_{\kappa}(r,s)/kT}$, where

$$U_{\kappa}(r,s) = U(r) + \sum_{\alpha=1}^{N_{\nu}} \frac{\kappa_{\alpha}}{2} \left[q_{\alpha}(r) - s_{\alpha} \right]^{2}$$
 (39)

and Ξ_{κ} is a κ -dependent normalising constant. These equations suggest that the potential of mean force $\phi(s)$ can be estimated by assigning a mass $m_{s_{\alpha}}$ and a momentum $p_{s_{\alpha}}$ to each s_{α} , thus turning s into a set of extended phase-space dynamical variables [34,46]. The potential energy of this extended phase-space system is defined as in Equation (39). This enables us, in principle, to calculate $\rho_{\kappa}(s)$ by collecting a histogram from a constant-NVT simulation of this extended system. In most situations, however, high free energy barriers render such a scheme impractical and require strategies for enhancing the sampling of the s-subspace. Examples are the driven adiabatic free energy dynamics (d-AFED) [26,27] method, also known as temperature-accelerated molecular dynamics [25] (TAMD), the extended-Lagrangian variants [29] of the metadynamics method [47] and its well-tempered extension [29,48], as well as the extendedsystem adaptive biasing force (eABF) method [49] and its generalised version (egABF) [50]. A particularly efficient way of generating $\phi(s)$ is through the unified free energy dynamics (UFED) method [28,51], which combines d-AFED/TAMD [25,27] with Metadynamics [47]. By also adding the SIN(R) method [13] to this combination, Chen and Tuckerman [34] were able to perform UFED calculations using very large time steps without observing resonance artifacts. Here, we replace SIN(R) by the simpler massive Nosé-Hoover-Langevin method in its regulated version described in Section 3.2.

The defining feature of d-AFED/TAMD is an adiabatic decoupling between the coarse-grained variables s and the physical coordinates r, with the former moving on a time scale much slower than the latter, so that the former can be thermalised at a temperature $T_s > T$. This becomes possible by assigning large masses, $m_{s_{\alpha}}$, to the coarse-grained variables, such that their dynamics becomes much slower than that of the physical coordinates. A consequence of the higher temperature is a more facile crossing of the free energy barriers, thus enabling enhanced sampling of the s-subspace. The regulated NHL equations of motion, as presented in Equations (31), are still valid for the physical degrees of freedom but with each force F_i now redefined as

$$F_{i} = -\frac{\partial U}{\partial r_{i}} - \sum_{\alpha=1}^{N_{v}} \kappa_{\alpha} (q_{\alpha}(r) - s_{\alpha}) \frac{\partial q_{\alpha}}{\partial r_{i}}.$$
 (40)

To each coarse-grained variable s_{α} , we associate a NHL thermostat with mass $Q_{\xi_{\alpha}}$ and momentum $p_{\xi_{\alpha}}$, so that equations of motion like Equations (31) can be written as

$$ds_{\alpha} = v_{s_{\alpha}} dt, \tag{41a}$$

$$dp_{s_{\alpha}} = \kappa_{\alpha}(q_{\alpha}(r) - s_{\alpha}) dt - \frac{p_{\xi_{\alpha}}}{Q_{\xi_{\alpha}}} m_{s_{\alpha}} v_{s_{\alpha}} dt, \quad \text{and}$$
(41b)

$$\mathrm{d}p_{\xi_{\alpha}} = \left(\frac{n+1}{n} m_{s_{\alpha}} v_{s_{\alpha}}^2 - kT_s\right) \mathrm{d}t \tag{41c}$$

$$-\gamma_s p_{\xi_{\alpha}} dt + \sqrt{2\gamma_s Q_{\xi_{\alpha}} kT_s} dW_{\xi_{\alpha}}, \qquad (41d)$$

where γ_s and $\mathrm{d}W_{\xi_\alpha}$ are the counterparts of γ and $\mathrm{d}W_{\eta_i}$ in Equation (31), and $v_{s_{\alpha}}$ is given by

$$v_{s_{\alpha}} = \sqrt{\frac{nkT_s}{m_{s_{\alpha}}}} \tanh\left(\frac{p_{s_{\alpha}}}{\sqrt{nm_{s_{\alpha}}kT_s}}\right).$$
 (42)

In the adiabatic limit, the physical degrees of freedom have sufficient time to thermalise around each point in the s-space in accordance with a conditional probability $\rho_{\kappa}(r|s) = \rho_{\kappa}(r,s)/\rho_{\kappa}(s)$ [25] such that the effective force acting on each variable s_{α} is

$$\bar{F}_{s_{\alpha}}(s) = -\left\langle \frac{\partial U_{\kappa}}{\partial s_{\alpha}} \right\rangle_{s} = -\frac{\int \left(\frac{\partial U_{\kappa}}{\partial s_{\alpha}}\right) e^{-U_{\kappa}(r,s)/kT} dr}{\int e^{-U_{\kappa}(r,s)/kT} dr}$$

$$= kT \frac{\partial}{\partial s_{\alpha}} \ln \int e^{-U_{\kappa}(r,s)/kT} dr = -\frac{\partial \phi_{\kappa}}{\partial s_{\alpha}}. \quad (43)$$

Therefore, the effective potential in the s-subspace is, in the adiabatic limit, exactly the desired PMF. Once the adiabatic condition is imposed, and the motion throughout this subspace is thermalised at temperature T_s , we can collect a histogram and generate $\phi_{\kappa}(s)$, up to an additive constant, via $-kT_s \ln \rho_{\kappa}^{\text{adb}}(s)$. Alternatively, we can compute the mean force expressed in Equation (43) at each point of a set of N_p configurations $\{(s_1, \ldots, s_{N_v})_k\}_{k=1,\ldots,N_p}$ and then reconstruct the PMF by expanding it in a basis set, e.g. radial, Fourier, etc. This approach yields results with better statistical accuracy [28,29].

Finally, the UFED method employs a historydependent biasing potential constructed on-the-fly as in the well-known Metadynamics scheme [47] but defined as a function of the coarse-grained variables s rather than of the physical coordinates r. Potential energy 'hills' in the form of Gaussian or similarly-shaped kernels are deposited at the current position s(t) at regular time intervals, so as to disfavor already visited regions of the s subspace. For Gaussian hills with height h and standard deviation σ_{α} for each direction, the added biasing potential is

$$U_{\text{bias}}(s,t) = h \sum_{k=1}^{\lfloor t/\tau \rfloor} e^{-\sum_{\alpha=1}^{N_{\nu}} [s_{\alpha}(t) - s_{\alpha}(k\tau)]^2/(2\sigma_{\alpha}^2)}, \quad (44)$$

where τ is the deposition period and $|\cdot|$ is the floor function. As shown by Chen et al. [28], adding this biasing potential does not alter the procedure for free-energy reconstruction using a basis set as long as the mean force $\bar{F}_{s_{\alpha}}(s)$ is generated via $\langle \kappa_{\alpha}(q_{\alpha}(r) - s_{\alpha}) \rangle_{s}$.

4. Numerical results

4.1. Liquid water simulations

In this section, we present molecular dynamics simulation results for liquid water at $T = 300 \,\mathrm{K}$ in order to assess whether the new equations of motion are capable of avoiding resonances and to compare them with the SIN(R) method in terms of performance. We employ the fully-flexible SPC-Fw model [52] with a smoothly truncated Lennard-Jones (LJ) potential defined as u(r) =

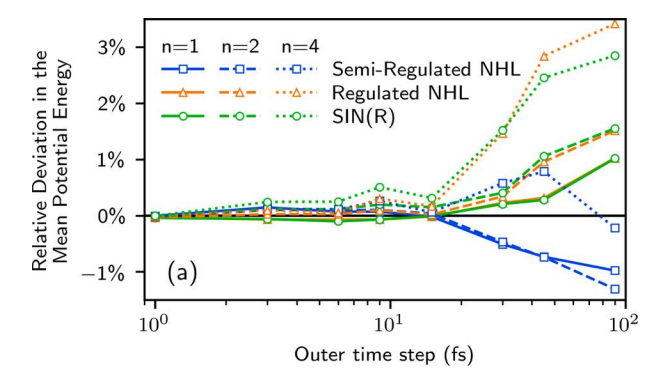
$$4\epsilon[(\sigma/r)^{12}-(\sigma/r)^6]S(\frac{r-r_s}{r_c-r_s})$$
, where

$$S(z) = \begin{cases} 1 & \text{if } z < 0\\ 1 - 10z^3 + 15z^4 - 6z^5 & \text{if } 0 \le z \le 1\\ 0 & \text{if } z > 1 \end{cases}$$
(45)

The switching and cutoff distances employed are, respectively, $r_s = 11 \text{ Å}$ and $r_c = 12 \text{ Å}$. Standard long-range corrections [44] are applied. In the case of electrostatic interactions, a damping parameter $\alpha = 0.2741 \,\text{Å}^{-1}$ is used for the real-space part of the Ewald sum, which is also truncated with the same r_c value employed for the LJ interactions. The reciprocal-space part is computed by the Particle Mesh Ewald (PME) method [53] with 48³ mesh points. The simulated system consists of N = 512 water molecules confined in a periodic cubic box whose edge length is L = 24.733 Å. This gives a density of $\rho = 1.012 \,\mathrm{g/cm^3}$, which is the room-temperature density reported for the water model in question [52]. The simulations were carried out using OpenMM [54] with customised integrators and interaction potentials. Further details can be found in Ref. [20].

We obtained reference results by performing a single-time scale integration with the BAOAB Langevin dynamics method [37,55], which is known to produce accurate coordinate distributions. The time step size and friction coefficient were, respectively, $\Delta t = 0.5$ fs and $\gamma = 1$ ps⁻¹. We computed average configurational properties, including the mean potential energy and radial distribution functions, from a simulation with 2.7 ns of equilibration and 24.3 ns of production.

For the SIN(R) method and regulated dynamics, we carried out multiple time-scale integration of the equations of motion (see Section 3.3). In most cases, the forces were split into three time scales by using the RESPA2 scheme [13,56,57]. For simplicity, we will refer to them as the short, middle, and long time scales. The forces assigned to the short time scale are the bonded interactions, namely the bond stretching and angle bending contributions, with a time-step size $\delta t_1 =$ 0.5 fs. The middle time scale included Lennard-Jones and full Coulomb interactions truncated at $r_c^{\text{in}} = 8 \text{ Å}$ and smoothly switched to zero from $r_s^{\text{in}} = 5 \text{ Å to } 8 \text{ Å}$. Here, the switching function $S(\frac{r-r_s^{\text{in}}}{r_c^{\text{in}}-r_s^{\text{in}}})$ multiplies the pairwise forces rather than the corresponding potential [20]. The time step size employed in the middle scale is $\delta t_2 = 3$ fs. Finally, the slowest forces are simply defined as the difference between the non-bonded interactions described above for the reference simulations (LJ + real-space Ewald + PME) and the middle-scale interactions just described. We evaluate the methods by employing several time-step sizes for integration in this outer time scale,



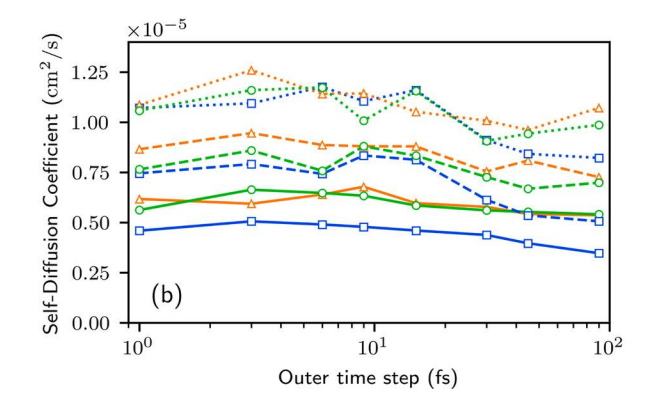


Figure 3. Results obtained from simulations of liquid water using the regulated dynamics methods and the SIN(R) method. Error bars were omitted for being as small as the symbols. Lines are simply intended as a guide for the eyes.

 $\delta t_3 = \Delta t$. It is worth noting that only two time scales, comprising, respectively, bonded and non-bonded interactions are used when $\Delta t \leq 3$ fs. Following Ref. [13], a high friction constant $\gamma = 0.1 \, \text{fs}^{-1}$ was used for the stochastic part and a characteristic time $\tau_c = 10 \, \text{fs}$ was employed for the Nosé-Hoover part of each thermostat. From this parameter we obtain $Q_1 = Q_2 = kT\tau_c^2$ for SIN(R) and $Q_\eta = nkT\tau_c^2$ for the regulated dynamics methods. Here, the n factor employed to compute Q_η is intended to allow an equitable comparison between methods that rely on different numbers of thermostats per degrees of freedom (see Appendix 2).

Figure 3 contains results of configurational and dynamical properties obtained for the water model in question. In Figure 3(a), we analyse the performance of the regulated NHL methods in reproducing the mean potential energy per molecule obtained from the reference BAOAB simulation with $\Delta t = 0.5$ fs and a single time scale, which is $\langle U \rangle^{\rm ref}/N = -42.794 \pm 0.006$ kJ/mol. We also compare the performance of the regulated dynamics methods with that of SIN(R). For this, we employed outer time steps of 1, 3, 6, 9, 15, 30, 45, and 90 fs. The total time in each simulation was 9 ns, with 1.8 ns of equilibration and 7.2 ns of production, during which the potential energy was sampled at every 90 fs.

We tested the methods with three different integer values for parameter *n*, which in SIN(R) translates as the number L of parallel thermostats per degree of freedom (see Appendix 2). The results are presented in the form of relative deviations $(\langle U \rangle - \langle U \rangle^{\text{ref}})/\langle U \rangle^{\text{ref}}$ as a function of the outer time step. The horizontal axis is plotted on a logarithmic scale for the sake of visual clarity. Error bars were computed via autocorrelation analysis [58], but they are omitted from Figure 3(a) as they have roughly the same size as the symbols.

As can be seen in Figure 3(a), all three methods exhibit very small deviations from the reference value, especially with $\Delta t \leq 15$ fs. Beyond this step size, average energies begin to diverge from the reference value as Δt increases. Nevertheless, even for the largest employed time steps, the maximum observed deviations are around 1% for the semi-regulated NHL method and around 3% for the regulated NHL and SIN(R) methods. In fact, the regulated NHL and SIN(R) methods behave very similarly, with both exhibiting a positive divergence from the reference value as Δt increases. This is consistent with the fact that these methods are closely connected when n = L and completely equivalent when n = L = 1, as shown in Appendix 2. In the case of the semi-regulated NHL method, the divergence is negative when $n \le 2$ but becomes positive for larger n values. In fact, both regulated variants become equivalent to the massive NHL method in its standard form as $n \to \infty$. Overall, the regulated NHL method exhibits the best performance when $\Delta t \leq 15$ fs, but the semi-regulated version exhibits the smallest divergence for larger Δt values. The divergence observed as Δt increases can be understood as an artifact due to the time discretisation, whose extension depends on the particular set of equations of motion. Different forms of backward error analysis, which involve concepts such as shadow Hamiltonians and shadow work, have been employed recently to understand and to alleviate these artifacts in the case of single time-scale integrators [30,31,33,39,59]. Extending these concepts for studying multiple time-scale methods is an interesting topic for future investigation.

Figure 3(b) contains values of self-diffusion coefficients (D_S) obtained by using the Einstein relation and considering the mean-square displacements (MSD) of oxygen atoms for increasing lag times. The slope of the MSD curve was computed by fitting the values corresponding to lag times from 1.8 ns up to 5.4 ns. The D_S value obtained in Ref. [52] for the SPC-Fw model using a global thermostat was 2.32×10^{-5} cm²/s. It is known that massive thermostatting with a strong coupling has a marked damping effect on diffusion [60], which means that the values shown in Figure 3(b) are not supposed to reproduce the result of Ref. [52]. They are intended

to provide a basis for comparison between the methods in terms of dynamical behaviour, which has an impact in the mixing necessary for configurational sampling. In any case, we can see that all methods are able to keep the value of D_S approximately constant regardless of the outer time step size employed. For all methods, diffusivity improves as n increases, which is consistent with Equation (11) and the fact that the mean kinetic energy of each degree of freedom also increases with n. Finally, these results empirically validate the comparison in Appendix 2, showing that our proposed regulation mechanism achieves, in a mathematically simpler and computationally more efficient manner, the same dynamical effect of the isokinetic constraints employed in SIN(R).

A more stringent test for configurational property calculation consists in comparing radial distribution functions (RDFs). New simulations were used to compute the oxygen-oxygen, oxygen-hydrogen, and hydrogenhydrogen RDFs by storing atomic positions every 900 fs and binning interatomic distances from 1.2 Å to 5 Å in 100 bins. This time, the thermostat inertial parameter is independent of *n* and computed as $Q_{\eta} = kT\tau^2$, with $\tau =$ 10 fs. Results obtained from all methods in three selected cases are shown in Figure 4 for comparison. In the case of the reference BAOAB method [37,55] with a single time step size $\Delta t = 0.5$ fs, only a subset of the 100 points obtained for each RDF curve is presented. The criterion for inclusion is that, for any two consecutive points in a depicted sequence, the dimensionless squared distance $[\Delta r/(1 \text{ Å})]^2 + (\Delta \text{RDF})^2$ is never smaller than 0.01. For the multiple time-scale methods, we employed natural cubic spline interpolation in order to present the curves in Figure 4 as continuous functions denoted by lines in different colors (depending on the method) and styles (depending on the element pair).

All radial distribution curves in Figure 4 are very close to their corresponding reference results. In Figure 4(a), with results for $\Delta t = 6$ fs and n = 1, the curves obtained from all MTS methods are visually indistinguishable from each other. For $\Delta t = 30$ fs and n = 2, depicted in Figure 4(b), it is only possible to observe a subtle difference in the first peak of the H-H distribution (dotted lines). Finally, deviations become noticeable in Figure 4(c), which shows the results obtained with $\Delta t = 90 \,\text{fs}$ and n = 4. SIN(R) seems to deviate more from the reference results than do the regulated dynamics methods.

Going beyond the qualitative analysis of Figure 4, we can also compare the radial distribution functions in a quantitative and more comprehensive way. For this, we employ the L1-error $\zeta = \frac{1}{n_b} \sum_{i=1}^{n_b} |g_i - g_i^*|$, where n_b is the number of bins, g_i is the RDF evaluated for a bin i,

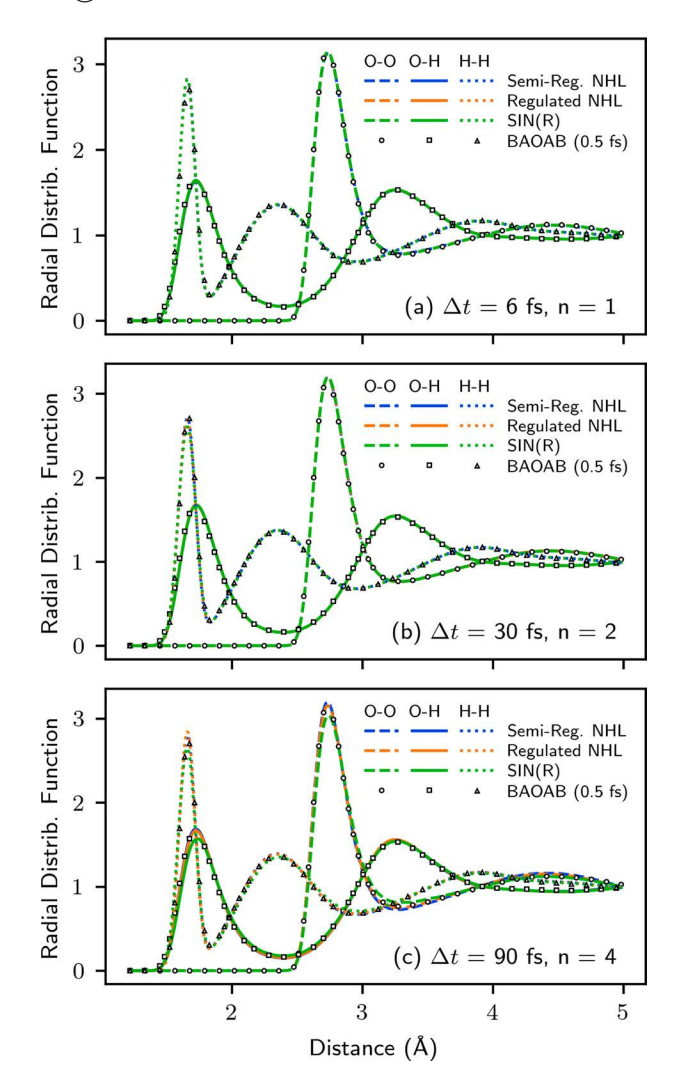


Figure 4. Radial distributions functions for oxygen-oxygen (O-O), oxygen-hydrogen (O-H), and hydrogen-hydrogen (H-H) intermolecular pairs for the fully-flexible SPC-Fw [52] water model at $\rho=1.012\,\mathrm{g/cm^3}$ and $T=300\,\mathrm{K}$.

and g_i^* is the particular g_i value obtained from the single time-step simulation used as a reference. In Figure 5, ζ is plotted against Δt for all simulated cases, with parts (a), (b), and (c) corresponding to oxygen-oxygen, oxygenhydrogen, and hydrogen-hydrogen pairs, respectively. A significant increase in ζ is seen in Figure 5 whenever Δt shifts from 1 to 3 fs, which are the cases with forces split into two time scales only. The distinction between these two cases is the number of substeps between consecutive impulses of non-bonded interactions, during which only bonded forces are updated. The shift from $\Delta t = 3$ to $\Delta t = 6$ fs marks the inclusion of a third time scale, when the non-bonded forces are split into short- and longrange contributions. As Figure 5 shows, such splitting has virtually no influence on the obtained RDFs. In fact, only small changes occur as Δt increases from 3 fs up to 15 fs. This behaviour is observed for all element pairs and for

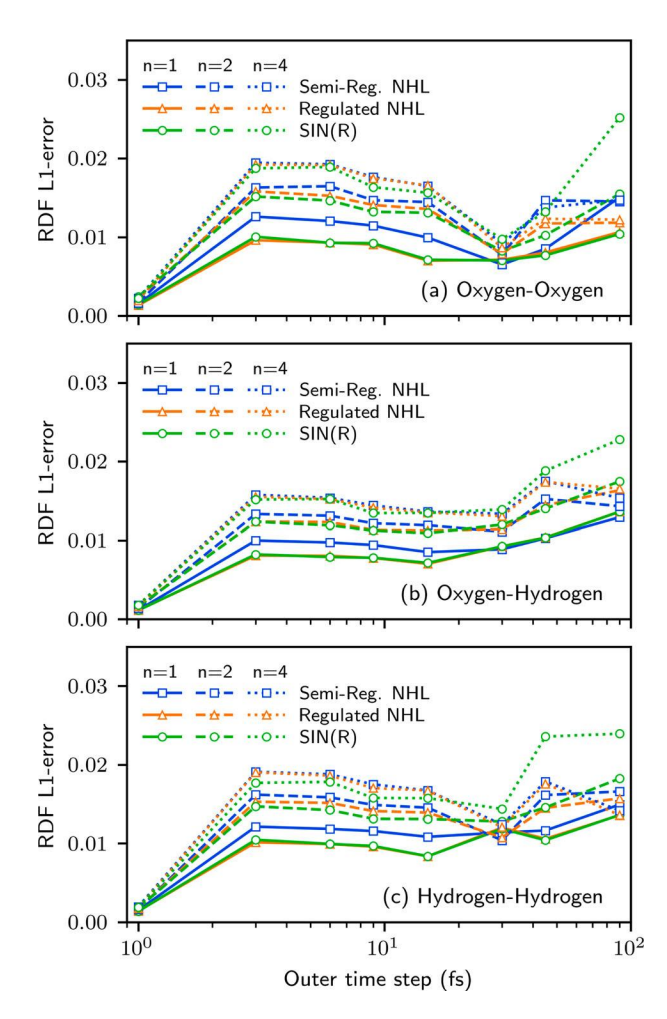


Figure 5. Means absolute deviations from reference radial distributions functions for oxygen-oxygen (O-O), oxygen-hydrogen (O-H), and hydrogen-hydrogen (H-H) intermolecular pairs for the fully-flexible SPC-Fw [52] water model at $\rho=1.012\,\mathrm{g/cm^3}$ and $T=300\,\mathrm{K}$.

all simulation methods. Therefore, the occurrence of a sharp initial departure of each RDF from its counterpart derived from a single time-step simulation is intrinsic to the employed force splitting and update frequencies.

Finally, as mentioned in Section 2.2, we investigate the use of the alternative Hamiltonian defined in Equation (12). Recall that this Hamiltonian promotes speed regulation while also satisfying the standard equipartition theorem regardless of the value of parameter n. In Figure 6, we show results for relative deviations of the mean potential energy. Here, the inertial parameter of the thermostat is also independent of n. In contrast to Figure 3(a), we observe large deviations from the reference value even for small outer time steps, which corroborates the discussion in Section 2.2. Therefore, use of the Hamiltonian in Equation (12) instead of that in Equation (4) for achieving regulation is not recommended.

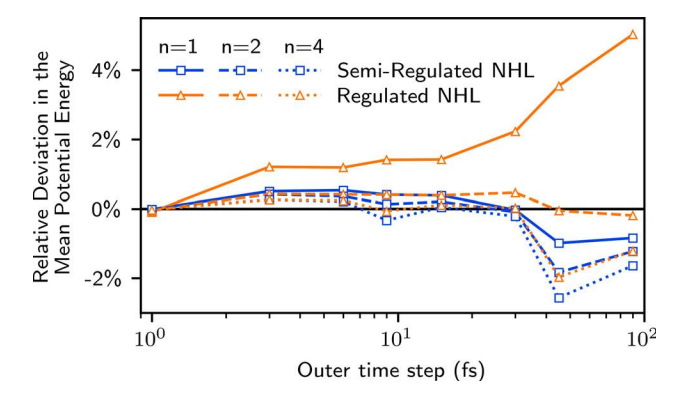


Figure 6. Results obtained from simulations of liquid water using alternative forms for the regulated dynamics methods obtained from the Hamiltonian $\mathcal{H}_n^{\text{eqp}}$, defined in Equation (12), which yields standard kinetic energy equipartition regardless of the value of the parameter n. Error bars were omitted for being as small as the symbols. Lines are simply guides for the eyes.

4.2. Ramachandran free-energy surface of alanine dipeptide in aqueous solution

In this section, we consider a more challenging application for the regulated dynamics approach. As described in Section 3.4, we use it in conjunction with the Unified Free Energy Dynamics (UFED) method [28] in order to perform enhanced sampling and compute free energy surfaces with respect to a set of collective variables. Our system of choice is an alanine dipeptide in aqueous solution, with the backbone dihedral angles ϕ and ψ chosen as the collective variables driven via the enhanced sampling. This is a suitable benchmark for the proposed method because of its well-studied and well-known behaviour. As in Section 4.1, we employed the fully-flexible SPC-Fw force field [52] for treating the explicit solvent. In the case of the dipeptide, we tested two different members of the AMBER (Assisted Model Building with Energy Refinement) family of force fields for proteins, specifically, ff03 [61] and ff14SB [62]. Vymětal and Vondrášek [63] tested the former and a predecessor of the later (ff99SB [64]), among other force fields, using a conventional metadynamics approach to perform the same type of calculation done here. Tzanov et al. [65] also tested ff99SB along with other force fields in a comparative study using d-AFED.

In the present study, we follow all simulation details presented in Section 4.1, with additional ones as now described. First, the proper dihedrals in the dipeptide contribute to the system energy in the form of a periodic torsion potential, which we assign to the short time scale, as well as the AMBER-type scaling of non-bonded interactions between 1–4 pairs [61], which we split into the middle and long time scales (as with all other non-bonded contributions). Second, we assign to the short time scale the harmonic potential terms such as those in

Equation (39), here involving the collective variables ϕ and ψ and their related extended phase-space variables s_{ϕ} and s_{ψ} , respectively. This is due to the high force constant κ required for generation of collective-variable free energy surface, as explained in Section 3.4. Third, the biasing potential is approximated by a two-dimensional, periodic cubic spline interpolation with 101×101 grid points uniformly spaced in the square $[-\pi, \pi]^2$. This spline is continuously updated by depositing a von Mises kernel

$$U_{\text{bias}}(s,t) = h \sum_{k=1}^{\lfloor t/\tau \rfloor} e^{-\sum_{\alpha=1}^{N_{\nu}} \frac{1 - \cos(s_{\alpha}(t) - s_{\alpha}(k\tau))}{\sigma_{\alpha}^{2}}}, \quad (46)$$

every $\tau=600\,\mathrm{fs}$, with parameters $h=2\,\mathrm{kJ/mol}$ and $\sigma_\phi=\sigma_\psi=\frac{\pi}{10}\,\mathrm{rad}$. This biasing potential is assigned to the middle scale because it only involves coarse-grained variables, whose dynamics are intentionally slow in the UFED framework and whose evaluation requires small computational effort when compared to that of longranged non-bonded interactions.

As stated in Ref. [29], the effective mass m_{eff} of each backbone dihedral angle in alanine dipeptide is $\sim 0.03 \,\mathrm{Da\cdot nm^2/rad^2}$. In a series of d-AFED/TAMD simulations with different masses m_s assigned to the coarse-grained variables, the ratio $\frac{m_{\rm s}}{m_{\rm eff}} \approx 10^3$ was found to yield a good compromise between adiabaticity and convergence rate [29]. Assuming that this finding carries over to the regulated dynamics method, we set $m_{s_{\phi}} =$ $m_{s_{\psi}} = 30 \,\mathrm{Da\cdot nm^2/rad^2}$ in all simulations. In addition, we set the force constants as $\kappa_{\phi} = \kappa_{\psi} = 10^3 \text{ kJ/mol} \cdot \text{rad}^2$, which were deemed in sufficiently high to yield accurate results [29]. The temperature of the extended space variables was kept at $T_s = 1500 \,\mathrm{K}$ by independent thermostats with the same characteristic time τ_c and friction constant γ employed for the physical degrees of freedom. In order to ensure full convergence of the free energy surfaces, each simulation was run for 36 ns.

For each employed protein force field, we carried out simulations with outer time steps Δt assuming values of 1, 3, 6, 15, 30, 60, and 120 fs. Each simulation was 36 ns long. In Figure 7, we show the free energy surfaces obtained from radial basis function analysis of the trajectories generated in some of these simulations. For this analysis, the (s_{ϕ}, s_{ψ}) space was split into 20 × 20 bins and the mean-force vector was estimated for each bin. These are represented in Figure 7 as black arrows. The radial basis functions are von Mises kernels with $\sigma = 4\pi/5$ rad supported at the bin centres with weights obtained by linear least-squares regression of the mean forces. The conformers identified in Figure 7 as

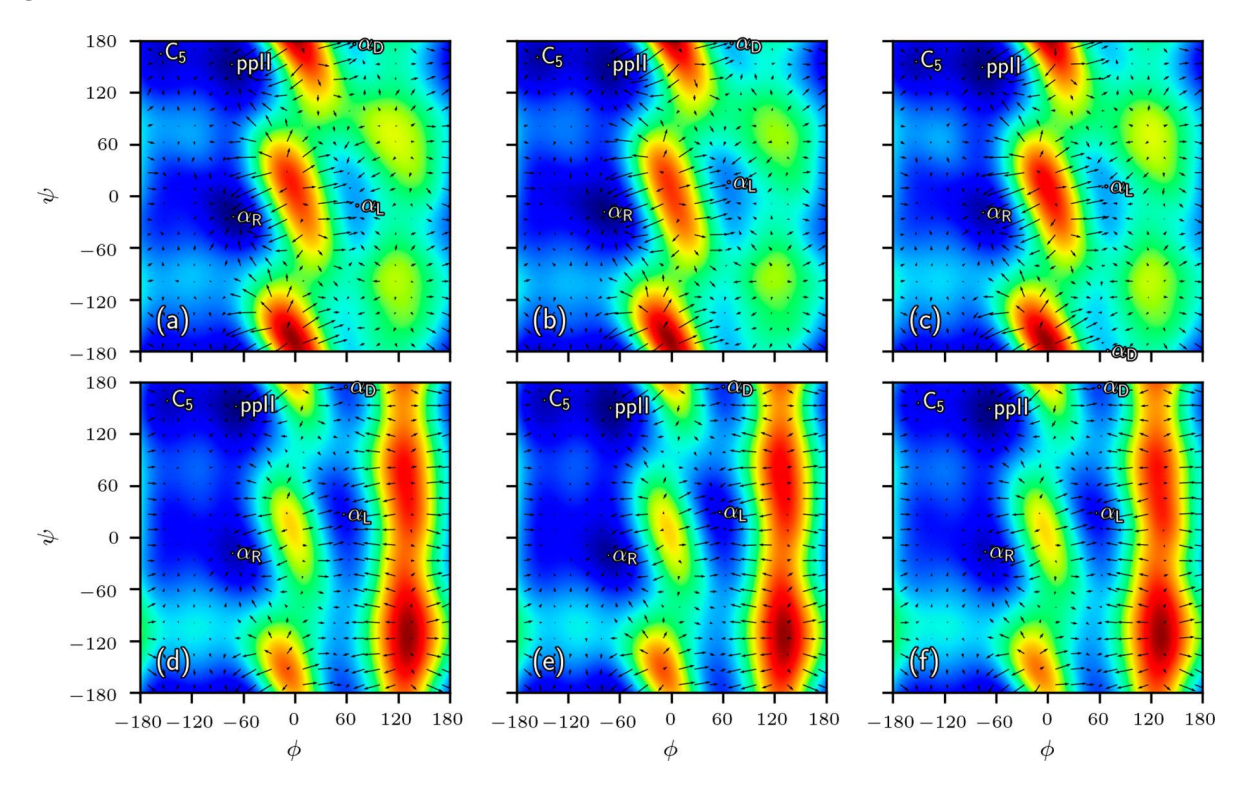


Figure 7. Ramachandran free energy surfaces obtained from regulated UFED simulations of alanine dipeptide in aqueous solution. The SPC-Fw [52] force field was used for the solvent and two versions of the AMBER force field were used for the solute, namely ff03 [61] (top row) and the ff14SB [62] (bottom row). The presented results were obtained using outer time steps Δt equal to 1 fs (left column), 30 fs (middle column), and 120 fs (right column).

 C_5 , ppII, α_R , α_L , and α_D were determined by Nelder-Mead minimisation of the computed free energy surfaces with the respective (ϕ, ψ) pairs as initial guesses: $(-150^{\circ}, 150^{\circ}), (-75^{\circ}, 150^{\circ}), (-60^{\circ}, -60^{\circ}), (55^{\circ}, 25^{\circ}),$ and $(60^{\circ}, -140^{\circ})$. It can be observed that, in all cases, the sampling enhancement promoted by UFED allowed a complete sweeping of the two-dimensional space, including the areas with the highest free energies. All important features of the free-energy landscape were correctly reproduced even with outer time steps as large as 120 fs, which can be observed by contrasting the results with those obtained for the same model using $\Delta t = 1$ fs.

5. Conclusion

In this paper, we have introduced the regulated dynamics approach, which achieves the very large time step gains in multiple time-scale molecular dynamics simulations achievable using the SIN(R) approach [13] and its deterministic variant [12] but within a Hamiltonian framework. The specific modification of the Hamiltonian provides a 'regulation' mechanism for controlling the resonance artifacts that plague multiple time-step algorithms in a way that avoids the need to impose isokinetic constraints or introduce additional phase-space variables. This new formulation not only simplifies the method, while still achieving very large outer time steps, it also reduces sampling errors and improves the overall performance of the algorithm. This fact was demonstrated in simulations of a flexible model of liquid water.

In addition, we showed how to formulate regulated dynamics as an enhanced sampling approach within the d-AFED and UFED frameworks, which, by extension, also includes its formulation with an extended-Lagrangian version of the popular metadynamics approach (achieved by setting $T_s = T$). The performance of the regulated dynamics scheme was then demonstrated in simulations of the solvated alanine dipeptide.

In future work, it will be interesting to explore the properties of the Hamiltonian in Equation 4 including dynamics produced by it, its quantum mechanical properties, and other mathematical aspects.

Acknowledgments

C.R.A.A. thanks the Federal University of Rio de Janeiro for a sabbatical leave and the New York University for a visiting scholar program membership.

Disclosure statement

No potential conflict of interest was reported by the author(s).



Funding

M.E.T acknowledges funding from the U.S. National Science Foundation, grant # CHE-1955381.

ORCID

Charlles R. A. Abreu http://orcid.org/0000-0002-6956-4045 *Mark E. Tuckerman* http://orcid.org/0000-0003-2194-9955

References

- [1] H. Grubmüller, H. Heller, A. Windemuth and K. Schulten, Mol. Simul. 6, 121 (1991). doi:10.1080/08927029108022-
- [2] M. Tuckerman, B.J. Berne and G.J. Martyna, J. Chem. Phys. 97, 1990 (1992). doi:10.1063/1.463137.
- [3] G.J. Martyna, M.E. Tuckerman, D.J. Tobias and M.L. Klein, Mol. Phys. 87, 1117 (1996). doi:10.1080/00268979-600100761.
- [4] J.J. Biesiadecki and R.D. Skeel, J. Comput. Phys. 109, 318 (1993). doi:10.1006/jcph.1993.1220.
- [5] T. Schlick, M. Mandziuk, R.D. Skeel and K. Srinivas, J. Comput. Phys. 140, 1 (1998). doi:10.1006/jcph.1998.5879.
- [6] Q. Ma, J.A. Izaguirre and R.D. Skeel, SIAM. J. Sci. Comput. 24, 1951 (2003). doi:10.1137/S1064827501399833.
- [7] B. García-Archilla, J.M. Sanz-Serna and R.D. Skeel, SIAM. J. Sci. Comput. 20, 930 (1998). doi:10.1137/S106482759-6313851.
- [8] R.D. Skeel and J.A. Izaguirre, in Computational Molecular Dynamics: Challenges, Methods, Ideas, edited by M. Griebel, D. E. Keyes, R. M. Nieminen, D. Roose, T. Schlick, P. Deuflhard, J. Hermans, B. Leimkuhler, A. E. Mark, S. Reich and R. D. Skeel (Springer Berlin Heidelberg, Berlin, Heidelberg, 1999), Vol. 4, pp. 318-331. doi:10.1007/978-3-642-58360-5_17.
- [9] J.A. Morrone, T.E. Markland, M. Ceriotti and B.J. Berne, J. Chem. Phys. 134, 014103 (2011). doi:10.1063/1. 3518369.
- [10] P. Minary, G.J. Martyna and M.E. Tuckerman, J. Chem. Phys. 118, 2510 (2003). doi:10.1063/1.1534582.
- [11] P. Minary, G.J. Martyna and M.E. Tuckerman, J. Chem. Phys. 118, 2527 (2003). doi:10.1063/1.1534583.
- [12] P. Minary, M.E. Tuckerman and G.J. Martyna, Phys. Rev. Lett. 93, 150201 (2004). doi:10.1103/PhysRevLett.93. 150201.
- [13] B. Leimkuhler, D.T. Margul and M.E. Tuckerman, Mol. Phys. 111, 3579 (2013). doi:10.1080/00268976.2013. 844369.
- [14] G.J. Martyna, M.L. Klein and M. Tuckerman, J. Chem. Phys. 97, 2635 (1992). doi:10.1063/1.463940.
- [15] A.A. Samoletov, C.P. Dettmann and M.A.J. Chaplain, J. Stat. Phys. 128, 1321 (2007). doi:10.1007/s10955-007-9365-2.
- [16] B. Leimkuhler, E. Noorizadeh and F. Theil, J. Stat. Phys. 135, 261 (2009). doi:10.1007/s10955-009-9734-0.
- [17] S. Nosé, J. Chem. Phys. 81, 511 (1984). doi:10.1063/1.447-
- [18] W.G. Hoover, Phys. Rev. A 31, 1695 (1985). doi:10.1103/ PhysRevA.31.1695.
- [19] R.C. Tolman, Phys. Rev. 11, 261 (1918). doi:10.1103/ PhysRev.11.261.

- [20] C.R.A. Abreu and M.E. Tuckerman, J. Chem. Theory. Comput. 16, 7314 (2020). doi:10.1021/acs.jctc.0c00698.
- [21] M.E. Tuckerman, C.J. Mundy and G.J. Martyna, Europhys. Lett. (EPL) 45, 149 (1999). doi:10.1209/epl/i1999-00139-0.
- [22] M.E. Tuckerman, Y. Liu, G. Ciccotti and G.J. Martyna, J. Chem. Phys. 115, 1678 (2001). doi:10.1063/1.1378 321.
- [23] Z. Zhang, X. Liu, Z. Chen, H. Zheng, K. Yan and J. Liu, J. Chem. Phys. 147, 034109 (2017). doi:10.1063/1.
- [24] Z. Zhang, X. Liu, K. Yan, M.E. Tuckerman and J. Liu, J. Phys. Chem. A 123, 6056 (2019). doi:10.1021/acs.jpca. 9b02771.
- [25] L. Maragliano and E. Vanden-Eijnden, Chem. Phys. Lett. 426, 168 (2006). doi:10.1016/j.cplett.2006.05.062.
- [26] L. Rosso, P. Mináry, Z. Zhu and M.E. Tuckerman, J. Chem. Phys. 116, 4389 (2002). doi:10.1063/1.1448491.
- [27] J.B. Abrams and M.E. Tuckerman, J. Phys. Chem. B 112, 15742 (2008). doi:10.1021/jp805039u.
- [28] M. Chen, M.A. Cuendet and M.E. Tuckerman, J. Chem. Phys. 137, 024102 (2012). doi:10.1063/1.4733389.
- [29] M.A. Cuendet and M.E. Tuckerman, J. Chem. Theory. Comput. 10, 2975 (2014). doi:10.1021/ct500012b.
- [30] M.P. Eastwood, K.A. Stafford, R.A. Lippert, M. Ø. Jensen, P. Maragakis, C. Predescu, R.O. Dror and D.E. Shaw, J. Chem. Theory Comput. 6, 2045 (2010). doi:10.1021/ct9002916.
- [31] R.L. Davidchack, J. Comput. Phys. 229, 9323 (2010). doi:10.1016/j.jcp.2010.09.004.
- [32] A.J. Silveira and C.R.A. Abreu, J. Chem. Phys. 147, 124104 (2017). doi:10.1063/1.5003636.
- [33] A.J. Silveira and C.R.A. Abreu, J. Chem. Phys. 150, 114110 (2019). doi:10.1063/1.5085441.
- [34] P.-Y. Chen and M.E. Tuckerman, J. Chem. Phys. 148, 024106 (2018). doi:10.1063/1.4999447.
- [35] M.J. Uline, D.W. Siderius and D.S. Corti, J. Chem. Phys. 128, 124301 (2008). doi:10.1063/1.2889939.
- [36] Y. Liu and M.E. Tuckerman, J. Chem. Phys. 112, 1685 (2000). doi:10.1063/1.480769.
- [37] B. Leimkuhler and C. Matthews, J. Chem. Phys. 138, 174102 (2013). doi:10.1063/1.4802990.
- [38] D. Li, X. Han, Y. Chai, C. Wang, Z. Zhang, Z. Chen, J. Liu and J. Shao, J. Chem. Phys. 147, 184104 (2017). doi:10.1063/1.4996204.
- [39] J. Fass, D. Sivak, G. Crooks, K. Beauchamp, B. Leimkuhler and J. Chodera, Entropy 20, 318 (2018). doi:10.3390/ e20050318.
- [40] B. Leimkuhler and C. Matthews, Molecular Dynamics With Deterministic and Stochastic Numerical Methods, Interdisciplinary Applied Mathematics, Vol. 39 (Springer International Publishing, Cham, 2015). doi:10.1007/978-3-319-16375-8.
- [41] H.F. Trotter, Proc. Amer. Math. Soc. 10, 545 (1959). doi:10.1090/S0002-9939-1959-0108732-6.
- [42] M. Suzuki, Commun. Math. Phys. 51, 183 (1976). doi:10.1007/BF01609348.
- [43] G. Strang, SIAM J. Numer. Anal. 5, 506 (1968). doi:10. 1137/0705041.
- [44] M.E. Tuckerman, Statistical Mechanics: Theory and Molecular Simulation, Oxford Graduate Texts (Oxford University Press, Oxford, New York, 2010).

- [45] A. Sergi and M. Ferrario, Phys. Rev. E 64, 056125 (2001). doi:10.1103/PhysRevE.64.056125.
- [46] M. Chen, T.-Q. Yu and M.E. Tuckerman, Proc. Natl. Acad. Sci. 112, 3235 (2015). doi:10.1073/pnas.1418241112.
- [47] A. Laio and M. Parrinello, Proc. Natl. Acad. Sci. 99, 12562 (2002). doi:10.1073/pnas.202427399.
- [48] A. Barducci, G. Bussi and M. Parrinello, Phys. Rev. Lett. 100, 020603 (2008). doi:10.1103/PhysRevLett.100.020-603.
- [49] A. Lesage, T. Lelièvre, G. Stoltz and J. Hénin, J. Phys. Chem. B 121, 3676 (2017). doi:10.1021/acs.jpcb.6b10055.
- [50] T. Zhao, H. Fu, T. Lelièvre, X. Shao, C. Chipot and W. Cai, J. Chem. Theory Comput. 13, 1566 (2017). doi:10.1021/acs.jctc.7b00032.
- [51] M. Chen, M.A. Cuendet and M.E. Tuckerman, J. Chem. Phys. 139, 069901 (2013). doi:10.1063/1.4817782.
- [52] Y. Wu, H.L. Tepper and G.A. Voth, J. Chem. Phys. 124, 024503 (2006). doi:10.1063/1.2136877.
- [53] T. Darden, D. York and L. Pedersen, J. Chem. Phys. 98, 10089 (1993). doi:10.1063/1.464397.
- [54] P. Eastman, J. Swails, J.D. Chodera, R.T. McGibbon, Y. Zhao, K.A. Beauchamp, L.-P. Wang, A.C. Simmonett, M.P. Harrigan, C.D. Stern, R.P. Wiewiora, B.R. Brooks and V.S. Pande, PLoS Comput. Biol. 13, e1005659 (2017). doi:10.1371/journal.pcbi.1005659.
- [55] B. Leimkuhler and C. Matthews, Appl. Math. Res. Express 2013, 34 (2013). doi:10.1093/amrx/abs010.
- [56] R. Zhou, E. Harder, H. Xu and B.J. Berne, J. Chem. Phys. 115, 2348 (2001). doi:10.1063/1.1385159.
- [57] J.A. Morrone, R. Zhou and B.J. Berne, J. Chem. Theory Comput. 6, 1798 (2010). doi:10.1021/ct100054k.
- [58] J.D. Chodera, W.C. Swope, J.W. Pitera, C. Seok and K.A. Dill, J. Chem. Theory Comput. 3, 26 (2007). doi:10.1021/ct0502864.
- [59] D.A. Sivak, J.D. Chodera and G.E. Crooks, Phys. Rev. X 3, 011007 (2013). doi:10.1103/PhysRevX.3.011007.
- [60] J.E. Basconi and M.R. Shirts, J. Chem. Theory Comput. 9, 2887 (2013). doi:10.1021/ct400109a.
- [61] Y. Duan, C. Wu, S. Chowdhury, M.C. Lee, G. Xiong, W. Zhang, R. Yang, P. Cieplak, R. Luo, T. Lee, J. Caldwell, J. Wang and P. Kollman, J. Comput. Chem. 24, 1999 (2003). doi:10.1002/jcc.10349.
- [62] J.A. Maier, C. Martinez, K. Kasavajhala, L. Wickstrom, K.E. Hauser and C. Simmerling, J. Chem. Theory Comput. 11, 3696 (2015). doi:10.1021/acs.jctc.5b00255.
- [63] J. Vymětal and J. Vondrášek, J. Phys. Chem. B 114, 5632 (2010). doi:10.1021/jp100950w.
- [64] V. Hornak, R. Abel, A. Okur, B. Strockbine, A. Roitberg and C. Simmerling, Proteins Struct. Funct. Bioinform. 65, 712 (2006). doi:10.1002/prot.21123.
- [65] A.T. Tzanov, M.A. Cuendet and M.E. Tuckerman, J. Phys. Chem. B 118, 6539 (2014). doi:10.1021/jp500193w.

Appendices

Appendix 1. Momentum and velocity distributions in a canonical ensemble with the regulating Hamiltonian

In an NVT ensemble with the regulating Hamiltonian \mathcal{H}_n , defined in Equation (4), the probability of each momentum p_i

is proportional to $e^{-n \ln \cosh[p_i/\sqrt{nm_ikT}]}$. Thus,

$$\rho_n(p_i) = \frac{1}{C_n} \operatorname{sech}^n \left(\frac{p_i}{\sqrt{n m_i k T}} \right), \tag{A1}$$

where C_n is a normalisation constant. Because the velocity v_i is a monotonic function of p_i , it is straightforward to obtain the velocity probability density $\varrho_n(v_i)$. Considering that, according to Equation (8),

$$f(v_i) = p_i = m_i c_i \operatorname{arctanh}\left(\frac{v_i}{c_i}\right),$$
 (A2)

the relation between the two probability densities is given by $\varrho_n(v_i) = |f'(v_i)|\rho_n(f(v_i))$, where

$$f'(v_i) = \frac{\mathrm{d}p_i}{\mathrm{d}v_i} = m_i \left(1 - \frac{v_i^2}{c_i^2}\right)^{-1}.$$
 (A3)

Therefore

$$\varrho_n(\nu_i) = \frac{m_i}{C_n} \left(1 - \frac{\nu_i^2}{c_i^2} \right)^{-1} \operatorname{sech}^n \left[\operatorname{arctanh} \left(\frac{\nu_i}{c_i} \right) \right]. \quad (A4)$$

Because $\operatorname{sech}(\operatorname{arctanh}(y)) = (1 - y^2)^{\frac{1}{2}}$ and due to the maximum speed c_i , we have that

$$\varrho_n(v_i) = \begin{cases} \frac{m_i}{C_n} \left(1 - \frac{v_i^2}{c_i^2} \right)^{\frac{n}{2} - 1} & \text{if } v_i^2 \le c_i^2 \\ 0 & \text{otherwise} \end{cases}$$
 (A5)

Finally, we can use the fact that $\int_{-c_i}^{c_i} \varrho_n(v_i) dv_i = 1$ in order to determine an expression for the constant C_n . By changing variables from v_i to $z = v_i/c_i$, we obtain

$$\frac{m_i c_i}{C_n} = \frac{1}{\int_{-1}^{1} (1 - z^2)^{\frac{n}{2} - 1} dz} = \frac{\Gamma\left(\frac{n+1}{2}\right)}{\Gamma\left(\frac{n}{2}\right)\sqrt{\pi}},$$
 (A6)

Therefore,

$$\frac{1}{C_n} = \frac{1}{m_i c_i} \frac{\Gamma\left(\frac{n+1}{2}\right)}{\Gamma\left(\frac{n}{2}\right)\sqrt{\pi}} = \frac{\Gamma\left(\frac{n+1}{2}\right)}{\Gamma\left(\frac{n}{2}\right)\sqrt{\pi} n m_i k T}.$$
 (A7)

The same change of variables can be employed to evaluate the central moments of the velocity distribution, whose symmetry makes null all odd-order ones. The even-order moments can be obtained by evaluating

$$\begin{split} \langle z^{2m} \rangle &= \frac{\Gamma\left(\frac{n+1}{2}\right)}{\Gamma\left(\frac{n}{2}\right)\sqrt{\pi}} \int_{-1}^{1} z^{2m} (1-z^2)^{\frac{n}{2}-1} \, \mathrm{d}z \\ &= \frac{\Gamma\left(\frac{n+1}{2}\right)\Gamma\left(\frac{2m+1}{2}\right)}{\Gamma\left(\frac{n+2m+1}{2}\right)\sqrt{\pi}}, \end{split} \tag{A8}$$

where *m* is a positive integer. We, therefore, obtain the general formula for the 2*m*th central moment of the distribution, which is

$$\langle v_i^{2m} \rangle = \frac{\Gamma\left(\frac{n+1}{2}\right) \Gamma\left(\frac{2m+1}{2}\right) n^m}{\Gamma\left(\frac{n+2m+1}{2}\right) \sqrt{\pi}} \left(\frac{kT}{m_i}\right)^m. \tag{A9}$$

Equation (11) follows directly from making m = 1.

Appendix 2. Close connection to the Stochastic Isokinetic Nosé-Hoover method

As we mentioned in Section 2.2, a special case of our proposed Hamiltonian, specifically, $n \in \mathbb{N}$, generates a canonical ensemble whose velocity distribution equals that of an isokinetic ensemble [20] with *n* thermostats per degree of freedom. This already confirms a close relationship between the two methodologies. In this appendix, we further demonstrate that our second proposed set of equations of motion, that based on the special equipartition relation in Equation (11), also produces the same dynamics as the Stochastic Isokinetic Nosé-Hoover method [13] when n = 1.

We first eliminate p_i from Equation (28b) using Equations (9) and (29), from which we deduce that

$$\dot{v}_i = \frac{\mathrm{d}p_i}{\mathrm{d}v_i}\dot{p}_i = \left(1 - \frac{m_i v_i^2}{nkT}\right) \left(\frac{F_i}{m_i} - \frac{p_{\eta_i}}{Q_{\eta_i}}v_i\right). \tag{A10}$$

We next define a new variable $v_{1,i}$ and a new equation of motion for each degree of freedom i, which is

$$\dot{v}_{1,i} = -\frac{F_i v_i - \frac{p_{\eta_i}}{Q_{\eta_i}} m_i v_i^2}{nkT} v_{1,i}.$$
 (A11)

Note that this new equation does not alter the dynamics of the preexisting variables, meaning that each $v_{1,i}$ is a driven variable [21,22]. Moreover, if $v_{1,i}(0) = 0$, it will remain zero for all time. Otherwise, it will vary in time but never change signs, since its rate of change vanishes when its own value approaches zero. We now show that the same features are shared by a variable Φ_i defined as

$$\Phi_i = m_i v_i^2 + \frac{n}{n+1} Q_{1,i} v_{1,i}^2 - nkT, \tag{A12}$$

whose rate of change is $\dot{\Phi}_i = 2(m_i v_i \dot{v}_i + \frac{n}{n+1} Q_{1,i} v_{1,i} \dot{v}_{1,i})$. From Equations (A10)-(A12), it turns out that

$$\dot{\Phi}_i = -2 \frac{F_i \nu_i - \frac{p_{\eta_i}}{Q_{\eta_i}} m_i \nu_i^2}{nkT} \Phi_i, \tag{A13}$$

which has nearly the same form as Equation (A12). Therefore, if an initial condition is assigned for all $v_{1,i}$ so that $\Phi_i(0) = 0$, then the dynamics will proceed in such a way that, at all times, it satisfies

$$m_i v_i^2 + \frac{n}{n+1} Q_{1,i} v_{1,i}^2 = nkT.$$
 (A14)

This equation is an isokinetic condition. However, it is not a constraint once $v_{1,i}$ is not a true dynamical variable. Moreover, we can rewrite Equations (A10) and (A11), respectively, as

$$\dot{\nu}_i = \frac{F_i}{m_i} - \lambda_i \nu_i \quad \text{and} \tag{A15a}$$

$$\dot{v}_{1,i} = -(\lambda_i + \nu_{2,i})\nu_{1,i},\tag{A15b}$$

where $\lambda_i = \frac{1}{nkT}[F_iv_i - v_{2,i}(nkT - m_iv_i^2)]$ and $v_{2,i} = -\frac{p_{\eta_i}}{Q_{n_i}}$. If, in addition, we assume that the isokinetic condition actually holds, then we can write

$$\lambda_i = \frac{F_i \nu_i - \frac{n}{n+1} Q_{1,i} \nu_{2,i} \nu_{1,i}^2}{m_i \nu_i^2 + \frac{n}{n+1} Q_{1,i} \nu_{1,i}^2}.$$
 (A16)

Finally, we also rewrite Equation (31c) by taking into account the isokinetic condition and the fact that $p_{\eta_i} = -Q_{\eta_i} \nu_{2,i}$, which

$$dv_{2,i} = \frac{Q_{1,i}v_{1,i}^2 - nkT}{Q_{\eta_i}} dt - \gamma v_{2,i} dt - \sqrt{\frac{2\gamma kT}{Q_{\eta_i}}} dW_{\eta_i}.$$
 (A17)

By setting n = 1 and noting that $\pm dW_{\eta_i}$ results in the same random process, the equations above become identical to those of the SIN(R) method [13] with a single thermostat attached to each degree of freedom, that is, L = 1. It only happens that, in the SIN(R) method, Equations (A15) are written down first, and λ_i is then seen as a Lagrange multiplier, determined afterwards so as to satisfy Equation (A14), which in this case is actually an isokinetic constraint.

It is worth using the present analysis to reinterpret previous results. Figure 2 of Ref. [13] discusses the influence of parameters $Q_{1,i}$ and Q_{η_i} on the ability of the SIN(R) method to sample correctly a simple one-dimensional model. The investigation was carried out with L = 1, which means that $v_{1,i}$ behaved as a driven variable. In such a situation, the value of $Q_{1,i}$ is not supposed to affect the sampling process, and this is exactly what the aforementioned figure shows us.

Finally, we compare the regulated NHL dynamics of Section 3.2 with the SIN(R) method with multiple thermostats per degree of freedom. First, instead of defining a single variable $v_{1,i}$ for each i, we define n such variables $v_{1,i,k}$ and a new isokinetic equation as

$$m_i v_i^2 + \frac{n}{n+1} \sum_{k=1}^n Q_{1,i} v_{1,i,k}^2 = nkT.$$
 (A18)

If we use this equation to displace $m_i v_i^2$ from Equation (31c),

$$dv_{2,i} = \frac{\sum_{k=1}^{n} Q_{1,i} v_{1,i,k}^2 - nkT}{Q_{\eta_i}} dt - \gamma v_{2,i} dt - \sqrt{\frac{2\gamma kT}{Q_{\eta_i}}} dW_{\eta_i},$$
(A19)

which represents a single NHL thermostat coupled to all $v_{1,i,k}$ for $1 \le k \le n$. Due to Equation (A18), these are still intermediate variables with driven dynamics. In the SIN(R) method [13], however, massive thermostatting is employed at this level as well. With an independent NHL thermostat attached to each $v_{1,i,k}$, these variables start influencing the dynamics of the remaining ones. This is what distinguishes the SIN(R) method with L > 1 from the Regulated NHL dynamics with $n \in \mathbb{N}$ and n > 1. Although such a high degree of thermostatting granularity seems beneficial in terms of ergodicity, it bears a considerable computational overhead. Moreover, our results in Section 4 suggest that it might be unnecessary in practical situations.